Rydberg Atom Vector Electrometry

A thesis submitted in partial fulfillment of the requirement
for the degree of Bachelor of Science with Honors in
Physics from the College of William and Mary in Virginia,

by

William Jay Torg

Advisor: Prof. Irina Novikova

Prof. S. Mordijck

Prof. Daniel Cristol

Williamsburg, Virginia
May 19 2026

Contents

Acknowledgments

I would first like to offer tremendous thanks to my advisor, Dr. Irina Novikova, for her terrific mentorship over the past four years. From the classroom to the lab to our group cookouts, Dr. Novikova has made my time with William and Mary physics and the Quantum Optics group an incredibly positive experience. I also want to thank Dr. Eugeniy Mikhailov for his mentorship throughout my time in WM QOL. I've consistently enjoyed his jovial nature and problem-solving attitude.

I want to express immense appreciation for the newly minted Dr. Rob Behary, who has been invaluable part of my time in the Quantum Optics Group. Our work together began with a one-day assembly of a power-supply. Since then, we've collaborated on a year's worth of Rydberg electrometry experimentation, during which time Rob's good-natured optimism ("5 papers by the end of the summer") made every moment more enjoyable. Without Rob, I don't think this project would've succeeded.

Additionally, I want to thank Owen Rollins and Kalea Wen for their camraderie throughout the past 3-4 years. Owen and Kalea have proven to be incredibly helpful when I have a question concerning my lab work. More importantly, they are great friends.

Lastly, I'd like to thank the rest of the Quantum Optics Group for making these past four years unforgettable. More broadly, I'd like to thank the many professors I've had the privilege of learning from throughout my time here at William and Mary.

List of Figures

Abstract

We present progress towards the development of a non-invasive atomic electrometry method capable of full reconstruction of an electric field. Our vector measurements utilize ^{85}Rb atomic vapor and two-photon Electromagnetically Induced Transparency (EIT), with atoms coupled to a highly excited Rydberg state. Applied electric fields produce a DC stark shift of the Rydberg level which corresponds to a frequency shift of the EIT peak in the recorded spectra, enabling measurement of electric field magnitude. The populations of specific levels are polarization-dependent, enabling electric field direction measurement. We demonstrate sensitivity to these population effects, and describe how this sensitivity enables vector measurement of the electric field. Moreover, the application of a known magnetic field establishes a quantization axis, enabling us to measure electric field direction via relative detuning of EIT resonances.

Chapter 1

Introduction

In 1865, James Clerk Maxwell published a set of equations that unified electricity and magnetism and predicted the existence of electromagnetic waves. A few decades later, in 1887, Heinrich Hertz verified Maxwell's prediction by performing experiments that observed propagating electromagnetic radiation [1]. These initial developments by Maxwell and Hertz have resulted in widespread applications that are foundational to much of modern technology from telecommunications and satellite technology to medical imaging. To realize these near-ubiquitous applications, it is necessary to conduct electric field measurements. Historically, electromagnetic measurements have been conducted using probes or antenna which consist of a physical piece of metal. The measurement of current flowing through this metallic object is recorded and translated into electric field strength [2]. In order for these probes to make accurate measurements, they must be calibrated relative to a known field. However, establishing a known field for calibration requires a calibrated probe, which creates some seemingly inherent imprecision.

The calibrated probe method has other flaws. Beyond their need for tuning, probe antenna are prone to breaking and malfunction. In the context of physics research, physical probes can be even more disruptive. The probe is a physical metallic structure, and its presence in the region of measurement perturbs the electromagnetic

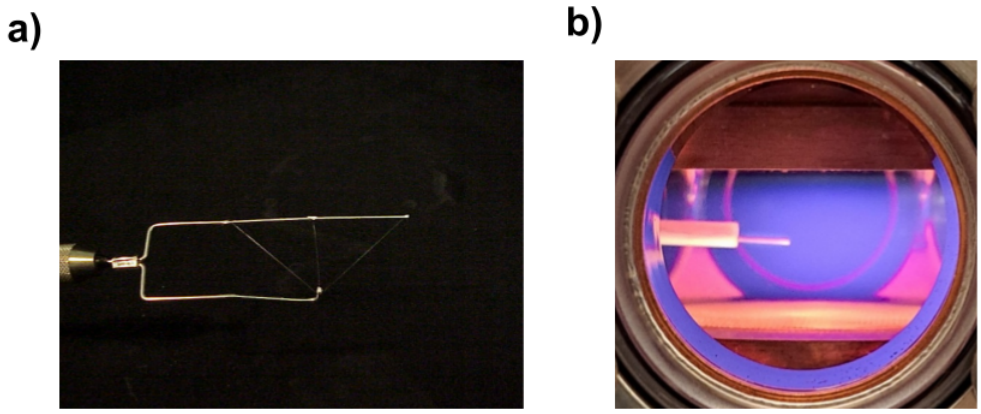

Figure 1.1: Conventional invasive probes employed for electric field measurements. (a) accelerator harp fork which is employed in charge particle beam diagnostics experiments at Jefferson Lab [3]. (b) Langmuir probe, which is employed in plasma physics experiments [4]. In both of these fields, a non-invasive electrometry technique would be preferable.

environment that is being measured. This invasive nature of physical probes impacts diagnostics in many areas of physics research. In particle physics experiments, a harp scanner (see Fig. 1.1a) is often used to detect the current profile of an electron beam. However, to utilize a harp scanner, experiments must be halted, and the scanner assembly must be placed within the beam path [3]. Moreover, the harp scanner is only viable at low currents and energies, which requires modification of the beam prior to measurement. A similar situation often occurs in plasma physics experiments, where Langmuir probes must be physically inserted into the plasma to gather electric field information (Fig. 1.1b). To better address these domains of research, a less invasive electrometry method is desired.

Atomic physics offers a compelling approach to the development of minimally-

invasive techniques for measuring electric and magnetic fields. Atomic energy levels are determined by fundamental constants and invariant for any atoms of a given element. As a result, atomic sensors are SI traceable and enable direct measurement of physical quantities without the need for an comparison with an external "known field". [2]. Moreover, atom-based sensing methods are optical in nature, enabling measurement without a perturbative conventional probe. Thus, atomic sensors present a minimally invasive alternative to conventional probes.

A key technique in atomic optical metrology is electromagnetically induced transparency (EIT), a coherent two-photon process that enables precise examination of atomic energy levels. EIT has been employed in a wide variety of atomic sensing applications. For example, atomic magnetometers that induce EIT in Rb vapor have achieved sensitivities of up to $2pT/\sqrt{Hz}$ [5]. In addition to magnetometry, EIT is also utilized for electric field measurement. EIT electrometry often involves the excitation of atoms to a highly-excited Rydberg state. These atoms are especially sensitive to external electric fields, and their response to these fields can be measured non-invasively. The use of Rydberg atoms for RF and DC electric field measurement is established [6].

However, most prior Rydberg electrometry research has been focused on the measurement of electric field magnitude, calculated from Stark-effect induced frequency shifts. Yet many of the industrial and research applications of Rydberg electrometry require full vector field reconstruction. To meet the demands of these widespread applications, Rydberg electrometry methods must also successfully measure direction.

This thesis seeks to demonstrate a non-invasive method for full vector reconstruction of electric field using Rydberg atoms and EIT. The thesis is structured as follows. In Chapter 2, we provide an overview of the theory associated with Rydberg EIT and highlight the relevance of EIT spectroscopy measurements for electric field measure-

ments. Here we include a discussion of our atomic modeling efforts. In Chapter 3, we describe our experimental configuration and discuss the methodology for measurement of electric field magnitude and direction. In Chapter 4, we discuss the implementation of transmission and fluorescence measurements, and their contribution to vector field reconstruction. In Chapter 5, we explain our result of full vector reconstruction of the electric field, describing advantages of our current strategy as well as future steps.

Chapter 2

Theoretical Foundations of Rydberg Electrometry

The ability to employ Rydberg atoms as "atomic antenna" for electric field sensing relies on a few distinct, yet interrelated physical phenomena. Rydberg atoms are highly sensitive to electric fields. This sensitivity is attributed to the Stark effect, which can be measured spectroscopically due to a coherent quantum effect known as Electromagnetically Induced Transparency. Moreover, the atomic populations within the Rydberg state are dependent on the orientation of light polarization and the external electric field. By recording EIT spectra, we are able to probe these atomic populations to discern information about the electric field direction. This chapter presents the conceptual foundations of our atomic method for full vector electric field reconstruction. Rydberg atoms are briefly illustrated. Then, the concept of a 3-level EIT ladder scheme is described. Next, the Stark effect is explained, with a focus on the Stark splitting of Rydberg energy levels enabling electric field magnitude measurement. Lastly, the polarization dependence of populations within the magnetic sublevels of the Rydberg state is illustrated as a means of determining electric field orientation.

2.1 Rydberg Atoms

The energy level spacing of a hydrogen-like atom follows the "Rydberg formula" [7]:

$$E_n \propto \frac{R_\infty}{n^2}$$

Where n is the principal quantum number and R_∞ is the Rydberg constant. Rydberg atoms have a single valence electron excited to a high principal quantum number, n resulting in a hydrogen-like atomic system. For a Rydberg atom (see Fig. 2.1(a)), the average orbital radius is given by $\langle r \rangle = n^2 a_0$, where a_0 is the Bohr radius [7]. The high principal quantum number of a Rydberg atom implies a large orbital radius for the valence electron, leading to high sensitivity to external electric fields. The atomic dipole moment $d \propto q \cdot r = e a_0 n^2$ is proportional to n^2. Atomic polarizability is proportional to radius and the difference in energy levels: $\alpha \propto \frac{r^2}{\Delta E}$. Since $r \propto n^2$ and $\Delta E \propto n^{-3}$ [8], the atomic polarizability scales with $\alpha \propto n^7$. This makes Rydberg atoms highly responsive to external electric fields, making them an ideal atomic medium for precision electrometry.

2.2 Rydberg EIT

Electromagnetically Induced Transparency is an interesting coherent effect because it makes atoms, which are normally opaque to incident laser light, transparent for optical fields that are near resonance with their atomic transitions. Figure 2.1b illustrates a 3-level two-photon EIT setup. A probe laser couples the long-lived, stable ground state $|g\rangle$ with an intermediate state $|e\rangle$ that is short-lived due to spontaneous emission. Additionally, a powerful coupling laser drives the transition from the intermediate state to the Rydberg state $|r\rangle$. Due to its high principal quantum number, the Rydberg state has a longer lifetime than the intermediate state. The Hamiltonian for

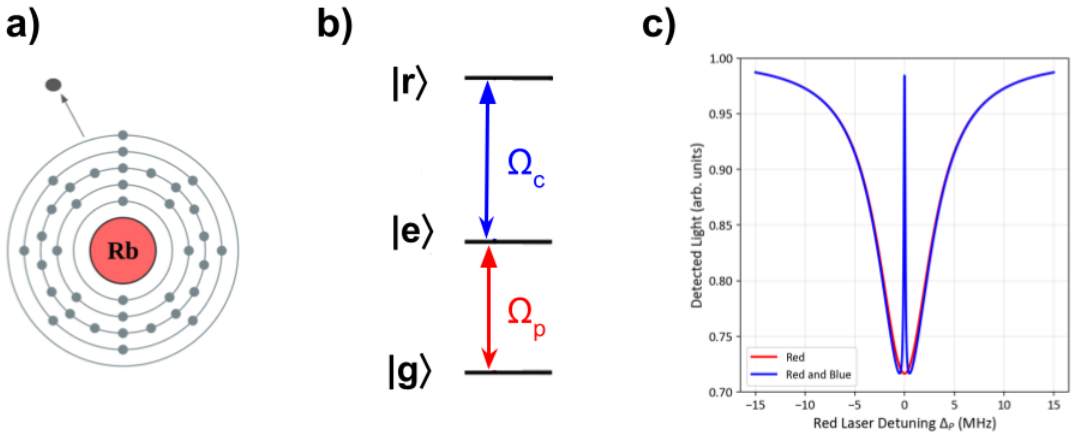

Figure 2.1: (a) Rubidium atom with one valence electron. When the atom's valence electron is excited to a high principal quantum number, it is said to be in a Rydberg state, and is incredibly sensitive to external electric fields. (b) Three-level ladder scheme of a Rubidium atom excited to the Rydberg state. A weak red probe laser couples the "ground state" $|g\rangle$ to the "intermediate state" $|e\rangle$. Additionally, a strong blue coupling laser couples the intermediate state $|e\rangle$ to the excited Rydberg state $|r\rangle$. (c) EIT transmission spectra. When only the probe laser is active, atoms absorb incoming light to excite the $|g\rangle \rightarrow |e\rangle$ transition, producing a broad dip in transmission centered on the $|g\rangle \rightarrow |e\rangle$ resonance. When both probe and coupling beams are turned on, we observe a narrow peak in transmission when both laser fields are on resonance. This corresponds to the "dark state" that gives rise to the EIT effect.

the three-level Rydberg EIT system given as [9]:

$$H = \frac{\hbar}{2}\begin{pmatrix} 0 & \Omega_p & 0 \\ \Omega_p & 2\Delta_p & \Omega_c \\ 0 & \Omega_c & 2(\Delta_p + \Delta_c) \end{pmatrix} \tag{2.1}$$

Ω_p is the probe Rabi frequency, which describes the coupling strength between the ground and intermediate state. Ω_c is the coupling Rabi frequency, which describes the coupling strength between the intermediate and excited Rydberg state. $\Delta_p = \omega_p - \omega_{ge}$ is the probe detuning, defined as the difference between the laser frequency ω_p and the atomic transition frequency ω_{ge} between the ground and intermediate state. $\Delta_c = \omega_c - \omega_{er}$ is the coupling detuning, defined as the difference between the laser frequency ω_c and the atomic transition frequency ω_{er} between the intermediate and excited Rydberg state. Finding the eigenstates of this Hamiltonian for a two-photon resonance condition where $\Delta_p + \Delta_c = 0$ yields an eigenstate that corresponds to an eigenvalue of 0 [9]:

$$|D\rangle = \frac{1}{\sqrt{\Omega_p^2 + \Omega_c^2}}(\Omega_c|g\rangle - \Omega_p|r\rangle) \implies \lambda_D = 0$$

This eigenstate, known as the "dark state", is a coherent superposition of the ground and Rydberg states of the three level system, and is responsible for the EIT effect[9]. Since the intermediate state of the three level system is absent from the dark state superposition (Eq.2.2), there are no losses of the atomic population from spontaneous emission of the intermediate state. Because $H|D\rangle = 0$, an atom in the dark state does not interact with the probe or coupling fields. In this decoupled state, atoms appear transparent to the incoming optical field.

The EIT effect is measured spectrographically. The dark state exists only when $\Delta_p + \Delta_c = 0$. When this two-photon resonance condition is met, a narrow transmission peak is produced in the recorded spectra (see Fig.2.1(c)). As either laser is detuned from resonance, the resonance condition is broken, and the dark state is

rendered inaccessible.

2.3 Stark Splitting

EIT resonance spectra grow more complicated in the context of an applied electric field. The Stark effect refers to the shifting and splitting of atomic energy levels when an external electric field acts upon an atomic system. More specifically, resonant frequencies of atomic transitions shift in proportion with the magnitude of the applied E-field. For a hydrogen atom,

$$\Delta f_{stark} = \frac{1}{2}\alpha E^2,$$

where f_{stark} is the resonant frequency of the atom, α is the polarizability of the atoms, and E is the applied electric field. For atoms excited to a Rydberg state, their valence electrons have high polarizability which leads to high sensitivity to Stark effects In the absence of a field, the fine structure of the Rydberg states are degenerate. The total angular momentum, J, that is associated with an atom is given by the sum of an atom's orbital angular momentum and spin angular momentum:

$$J = L + S$$

The magnetic quantum numbers m_j associated with a value of J range from $-J$ to J in integer steps. As a result, there are $2J + 1$ magnetic sublevels associated with any total angular momentum value. The application of an electric field partially lifts the degeneracy of these m_J sublevels. When considering the polarizability term from 2.3, it is clear that the energy level splitting exhibits $|m_J|^2$ dependence [10]:

$$\alpha = \alpha_0 + \frac{3m_J^2 - J(J+1)}{J(2J+1)}\alpha_2$$

where α_0 and α_2 are the scalar and tensor atomic polarizability, respectively. It is important to note that for a fixed atomic state, J, α_0 and α_2 are fixed. Therefore, the only possible means of breaking degeneracy is through the $|m_J|^2$ term. As a result, sublevels with the same $|m_J|$ value remain degenerate, leading to three distinct sublevels corresponding to the magnetic quantum numbers $m_J = \pm 1/2, \pm 3/2, \pm 5/2$ (see Fig. 2.2(a)).

Stark splitting is pivotal to our experiment. Figure 2.2 shows a simulated measurement, first with the electric field off and then with the external electric field activated. It can be observed that applying an external electric field breaks the degeneracy of the magnetic sublevels, resulting in three distinct peaks that are detuned from the central resonance by differing amounts depending on the m_J number associated with the peak. The detuning dynamics of the m_J sublevels is highly nonlinear. The numerical simulation of the atomic system can be done numerically using ARC software [11]. These simulations produce a Stark map, or "squid plot", that visualizes the calculated detunings for each of the m_J sublevel peaks over a continuous range of electric field values (measured in V/m). By recording the detunings of the m_J sublevels of the Rydberg state, and comparing these detunings with the simulated "squid plot" reference (pictured in Fig. 2.2c), we are able to estimate the magnitude of the applied electric field.

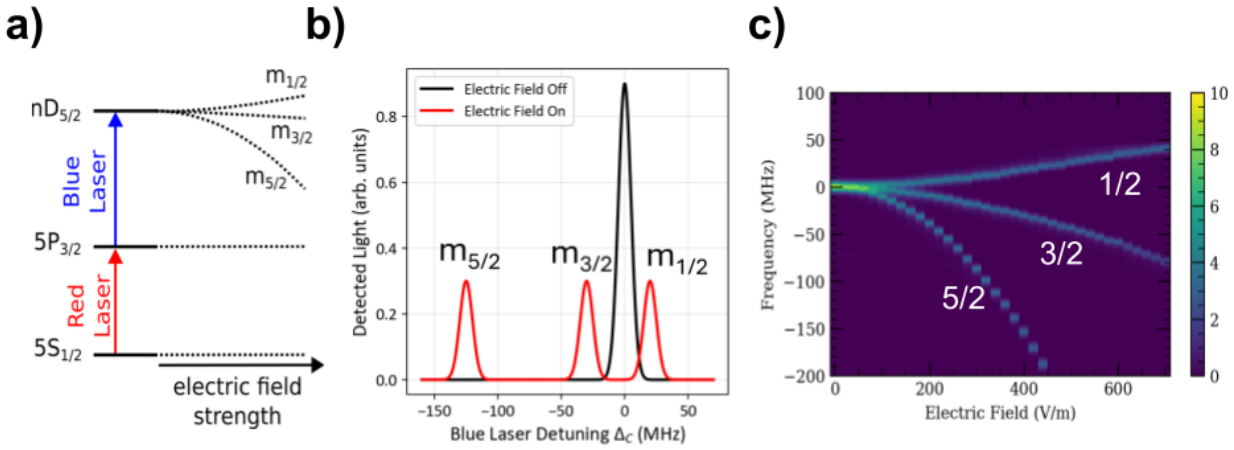

Figure 2.2: (a) Three-level ladder scheme upon the application of an external electric field. The different m_J sublevels of the Rydberg state detune away from the central resonance in a manner proportional to electric field strength. (b) Detunings represented in on our EIT spectra. With the field off there is one central resonance, but the different sublevels form distinct peaks upon the application of an external electric field. (c) "squid" plot that shows corresponding detunings of each magnetic sublevel with increasing electric field. These responses are nonlinear.

2.4 Polarization Dependence of Sublevel Populations

The magnetic sublevels $m_J = \pm 1/2, \pm 3/2, \pm 5/2$ emerge from the projection of the total angular momentum J onto the quantization axis. Here, by applying an external electric field, we define the quantization axis along the electric field direction. Our laser polarization then determines which of these sublevels can be populated. Selection rules determine that laser polarization parallel to the electric field (π polarization) drives $\Delta m_J = 0$ transitions, while circularly polarized light drives $\Delta m_J = \pm 1$ transitions. As a result, the populations of the Rydberg m_J sublevels, and the corre-

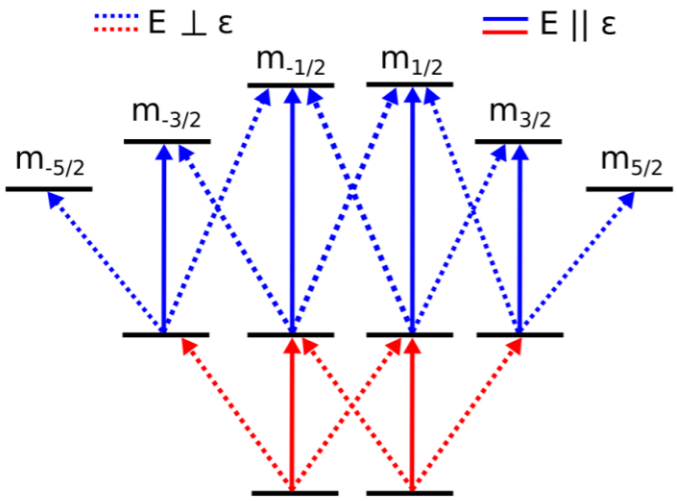

Figure 2.3: Allowed optical transitions for the cases when laser polarization is parallel (solid lines) or perpendicular (dashed lines) to electric field direction. When the polarization is neither parallel nor perpendicular, a mixture of these optical transitions is activated, leading to different population distributions depending on relative orientation between electric field and laser polarization.

sponding amplitudes of their associated EIT resonances, are determined by the choice of polarization orientation of the red and blue lasers. The simplified energy level diagram in Fig.2.3 demonstrates this relationship. If only π transitions are allowed, the $m_{\pm 5/2}$ state is inaccessible. However, when laser polarization is perpendicular to the electric field, we maximize the $m_{\pm 5/2}$ transition. We expect that by rotating the polarization and calculating the area of our EIT peaks, we should be able to determine the relative contributions of different transitions. This will enable the determination of electric field orientation.

Chapter 3

Atomic Model

This chapter explains the atomic modeling efforts behind this experiment. The atomic model was compared with our experimental measurements to investigate the validity of our results.

3.1 Motivation

Section 2.3 referenced the ARC software that was employed to establish an atomic reference that could be used to infer electric field magnitude. For electric field direction, a similar computational effort is required. However, to properly calculate polarization dependence, it is necessary to consider the hyperfine structure of Rubidium. This hyperfine structure has many different levels, leading to a highly complex array of possible atomic transitions. As a result, modeling the full atomic structure with all hyperfine transitions proved too computationally intensive for our resources. This limitation was later addressed by our collaborators at MITRE, who developed a full atomic model accounting for the complete hyperfine structure [6]. This section will discuss a simple atomic model that was constructed for comparison with our experimental results. Our simple model had deficiencies in comparison with our experimental results (see Secton 4.3), the origins of which were unclear. The MITRE model is too complicated to be described here, but demonstrates better alignment

with our experimental results. This indicates that the source of discrepancy between our model and the experimental data was largely due to the truncated hyperfine structure in our model, rather than any experimental error concerning the underlying physics.

3.2 Simple Atomic Model

Our simplified atomic model considers the polarization dependence (discussed in Section 2.4) of individual pathway transitions. It does so by weighting selection rule pathways based on the projection of left and right circular polarizations (σ_+, σ_- transitions) onto the atomic quantization axis. In our system, this quantization axis is set by the direction of the applied electric field. However, our polarization vector is initially expressed in the spherical basis of the electromagnetic field, while the electric field vector is expressed in Cartesian coordinates. In order to project the polarization vector onto the quantization axis, it is necessary for both of these vectors to be situated within the same reference frame. This need for comparison between polarization vector and electric field vector motivated the model geometry specifications described below.

3.2.1 Model Geometry

We begin by considering the system in the Cartesian coordinate space shown in Figure 3.1a. Then, given an electric field magnitude, as well as its theta and phi direction, we construct an electric field vector:

$$\hat{E} = E \begin{pmatrix} \sin\theta\cos\phi\hat{x} \\ \sin\theta\sin\phi\hat{y} \\ \cos\theta\hat{z} \end{pmatrix}$$

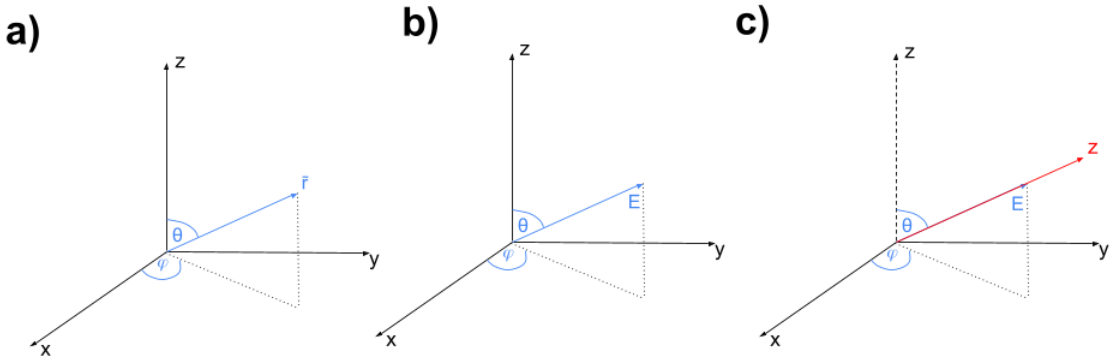

Figure 3.1: (a) General cartesian space. (b) Applied electric field vector in cartesian space. (c) Geometry used to orient atomic model. Frame is rotated so that the z axis aligns with our quantization axis set by the electric field direction.

We also take an input, θ_L that describes the polarization direction. Our polarization vector is initially given in the spherical basis of the electromagnetic field:

$$\hat{\epsilon} = \epsilon \begin{pmatrix} \frac{-\sin\theta_L}{\sqrt{2}}\hat{\sigma_+} \\ \frac{\sin\theta_L}{\sqrt{2}}\hat{\sigma_-} \\ \cos\theta_L\hat{\pi} \end{pmatrix}$$

We then employ a transformation matrix to convert the polarization vector to cartesian coordinates:

$$\begin{pmatrix} E_x \\ E_y \\ E_z \end{pmatrix} = T \begin{pmatrix} E_{\sigma+} \\ E_{\sigma-} \\ E_\pi \end{pmatrix}, \text{where } T = \begin{pmatrix} -\frac{1}{\sqrt{2}} & \frac{1}{\sqrt{2}} & 0 \\ -\frac{i}{\sqrt{2}} & -\frac{i}{\sqrt{2}} & 0 \\ 0 & 0 & 1 \end{pmatrix}$$

Now, with both the polarization and electric field vectors in cartesian space, a matrix rotation is performed using the Euler-Rodriguez formula [12]:

$$T_{Euler-Rodrigues} = \begin{pmatrix} a^2+b^2-c^2-d^2 & 2(bc-ad) & 2(bd+ac) \\ 2(bc+ad) & a^2+c^2-b^2-d^2 & 2(cd-ab) \\ 2(bd-ac) & 2(cd+ab) & a^2+d^2-b^2-c^2 \end{pmatrix}$$

To determine a, b, c, d, we need to define a rotation axis and determine the angle that the matrix will be rotated relative to that axis (referred to as the rotation angle). We define $\hat{u} = \frac{\hat{z}\times\hat{E}}{|\hat{z}\times\hat{E}|} = \frac{(-E_y, E_x, 0)}{\sqrt{E_x^2+E_y^2}}$. Next, we find our rotation angle relative to the rotation axis is given by $\phi_{rot} = \arccos E_z$. Given a rotation axis and angle, we define $a = \frac{\cos\phi_{rot}}{2}, b = u_x\frac{\sin\phi_{rot}}{2}, c = u_y\frac{\sin\phi_{rot}}{2}, d = u_z\frac{\sin\phi_{rot}}{2}$. Now we apply this rotation matrix to our polarization vector $\epsilon \rightarrow T_{Euler-Rodrigues}\epsilon$ into this new reference frame. Lastly, convert ϵ back into the spherical basis of the electromagnetic field: $\hat{\epsilon}_{(x,y,z)} \rightarrow \hat{\epsilon}_{(\sigma_+,\sigma_-,\pi)}$ to get the relative strength of each transition in a given polarization-electric field orientation.

3.2.2 Atomic Model Principles

Given an aligned geometry, we then solve for the amplitude of certain states using a "rate" model [6]. We calculate the total EIT transmission spectra as a sum of individual contributions from each possible excitation pathway [6]:

$$S(\Delta_C) = \sum_{m_{J_3}} S_{m_{J_3}} \exp\left(-\frac{[\Delta_C - \Delta f_{|m_J|}(E)]^2}{2\gamma_{EIT}^2}\right),$$

Here, Δ_C is the detuning of the coupling field, $\Delta f_{|m_J|}(E)$ is the Stark shifted frequency of each distinct $|m_J|$ peak, and γ_{EIT} is the width of the EIT resonance. $S_{m_{J_3}}$ represents the probability of a given transition pathway contribution to each $|m_J|$ peak, and is calculated as [6]:

$$S_{m_{J_3}} = \sum_{m_{F_1}}\sum_{m_{F_2}} d^2_{m_{F_1}\rightarrow m_{F_2}} d^2_{m_{F_2}\rightarrow m_{J_3}}. \tag{3.1}$$

where $d_{m_{F_1}\rightarrow m_{F_2}}$ and $d_{m_{F_2}\rightarrow m_{J_3}}$ are coefficients that are dependent on selection rules and the strength of laser polarization components. $d_{m_{F_1}\rightarrow m_{F_2}}$ details a given transition from ground to intermediate state, while $d_{m_{F_2}\rightarrow m_{J_3}}$ corresponds to a transition from intermediate to excited state. The probabilities associated with these calculations serve as weights in our simple, semi-analytical model. By inputting our system

geometry, we are able to project the strength of certain transitions,as well as the relative peak heights that would be expected on an EIT spectra. While this simple model is not perfectly accurate (see Fig.4.4), it is a reasonable approximation of system behavior.

Chapter 4

Uniform Field Experiments

Having established a model for the polarization-dependent EIT response in Rydberg atoms, this chapter applies it towards the investigation of electric field direction. First, the relatively simple case of a uniform electric field is considered. This chapter explains the experimental setup, then describing the process for recording EIT transmission measurements. These results are then compared with the output of the simple atomic model, demonstrating qualitative agreement, particularly in the case where polarizations are rotated together. The methods illustrated in this chapter demonstrate the potential for uniform field reconstruction through this technique.

4.1 Experimental Setup

Our experimental setup (Fig.4.1) consists of a vacuum chamber that contains built-in capacitor plates with 24mm plate separation. These capacitor plates generate a uniform electric field in the x direction. The vacuum chamber is filled ^{85}Rb vapor, and the EIT effect is produced by applying a bi-chromatic laser field to this alkali metal vapor. A 780nm probe field with 500μW power and approximately 0.3mm width couples the system's ground state ($5S_{1/2}$) to the intermediate excited state ($5P_{3/2}$). A 480nm coupling field with $50mW$ power and approx. 0.3mm width excites the optical transition from this intermediate state to the Rydberg state ($nD_{5/2}$). The two optical

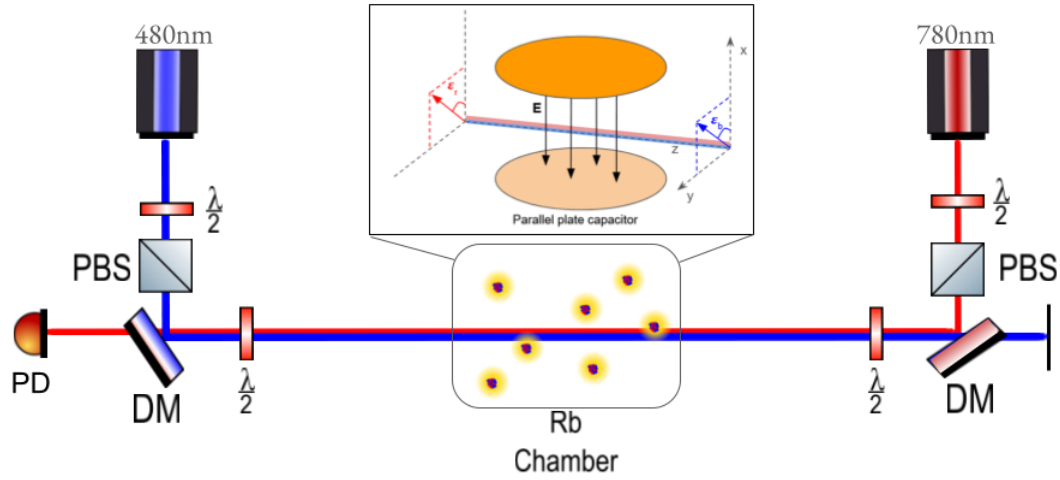

Figure 4.1: Illustration of the experimental setup used for uniform electric field measurements. A 480nm laser and 780nm laser are counter-propagated through the rubidium chamber. Polarization of each laser field is cleaned and aligned vertically through a half-waveplate and polarizing beam-splitter (PBS). Each beam reflects off a dichroic mirror before meeting another half-waveplate that assigns its input polarization. These polarizations are rotated, imitating electric field rotation in our static-field system. Red laser transmission is recorded on a photodetector. Note that laser polarization vectors for both the blue and red lasers, as well as their polarization angles, are defined as the angle between the polarization vector and the y-axis.

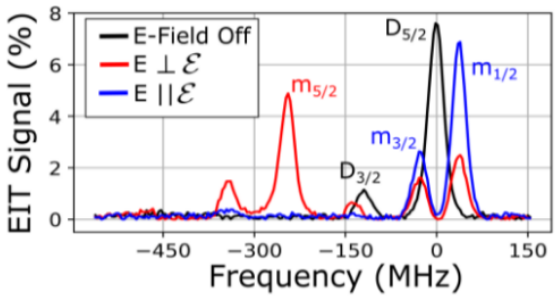

Figure 4.2: Sample EIT spectra measurement. The distinct m_J sublevels are apparent, and there are demonstrable changes in sublevel population depending on field orientation.

fields are linearly polarized parallel to the surface of a dichroic mirror through the use of a half-waveplate in combination with a polarizing beam splitter (see Fig. 4.1). This is done to prevent polarization distortion upon reflection. After reflection from the dichroic mirror, beam polarization is adjusted to the desired orientation through the use of an additional half-waveplate. The probe and coupling laser fields counter-propagate through the chamber, which partially cancels the Doppler shifts associated with each atom. The probe field transmission is then recorded on a photodetector. By fixing the coupling field on resonance and sweeping the frequency of the probe field across its resonant frequency, we are able to record an EIT spectrum (an example of which is shown in Fig.4.2). This method accounts for the total contribution of all Rb atoms across the laser beam, making it ideal for measurement of a uniform electric field.

4.2 Processing Transmission Spectra

Fig. 4.2 depicts a measurement of an EIT spectra recorded from transmission measurement. We begin our experiment by applying a fixed voltage that generates a static, uniform electric field (measured in V/m) within the vacuum chamber. From

our Stark map in Fig. 2.2, we expect to observe a specific separation between m_J-dependent sublevel resonances (measured in MHz). As expected, we observe noticeable splitting of EIT peaks due to Stark shifting of their corresponding Rydberg sublevels. In order to extract vector electric field information from our transmission

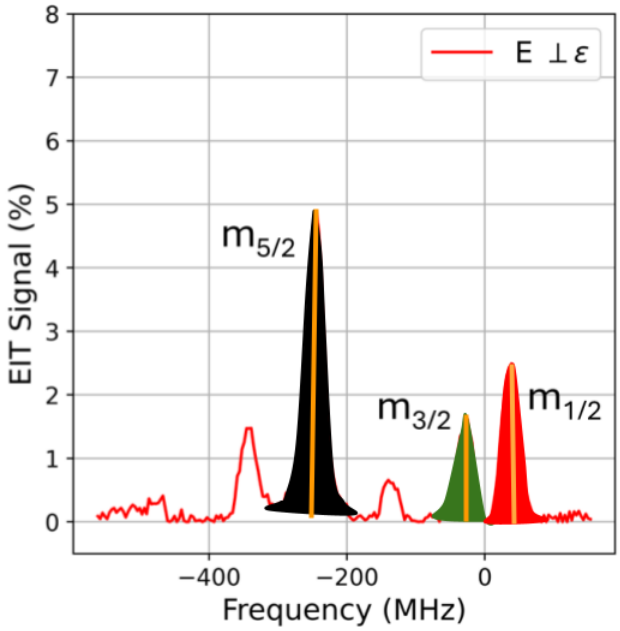

Figure 4.3: m_J sublevels shift in the presence of an applied electric field. Orange lines corresponding to the maximum peak height are obtained via comparison with the expected sublevel detunings from our calculated reference (Fig. 2.2c) After m_J sublevel peaks are located from the orange line fitting, peak area is calculated from Gaussian fitting of the resonance. This area is then used to determine the ϕ angle associated with the individual measurement. When combined, these measurement processes yield vector electric field reconstruction in the uniform field case.

spectra, we perform two varieties of peak-fitting analysis.

To extract magnitude, we measure the detunings of each EIT peak from the central resonance (See Fig. 4.3(a)). Then, using our "squid map" from Fig. 2.2 we are able to infer electric field magnitude. To extract direction information, we utilize the polarization dependence of Rydberg sublevel populations. By measuring the EIT peak area associated with each sublevel, we are able to predict the phi-dependence

of the electric field (see Fig. 4.3(b)). Peak area is defined as the amplitude of the peak multiplied by its full width at half maximum (FWHM) of the fitted peak shape. Peak area is preferred to peak height in these measurements due to its reduced sensitivity to potential field gradients. A field gradient causes atoms within the vapor cell to experience slightly different electric field magnitudes and, consequently, different detunings. This leads to a broadened peak, with decreased height. However, since peak area is calculated across the entire transmission peak, its value is conserved under broadening. This makes peak area preferable for counting total populations at a given m_J sublevel in the presence of potential gradients. In the case of a uniform electric field, the measurements provide both magnitude and direction information, yielding full vector field reconstruction.

4.3 Transmission Measurements

To obtain a rudimentary understanding of the dependence of EIT peaks on both the red and blue laser polarizations, the experimental polarization "map" (depicted in Fig.4.4) was constructed. To obtain these measurements, the probe field polarization was fixed at 0° while coupling field was varied between 0° and 180° at 10° increments. These measurements were repeated, varying the probe field polarization between 0° and 180° at 10° increments. These colormaps provide a visual representation of EIT peak areas for each m_J sublevel of the Rydberg state. Each pixel in each map corresponds to the peak area of a given m_J sublevel in a given orientation. We observe that peak areas, and therefore m_J sublevel populations, are dependent on the orientation of both the probe (ϕ_R) and coupling (ϕ_B) lasers. Since our experiments have a static electric field, this rotation of laser polarization is equivalent to changing the electric field direction. As a result, these colors maps demonstrate electric field sensitivity by these sublevels of the Rydberg state. We observe that the

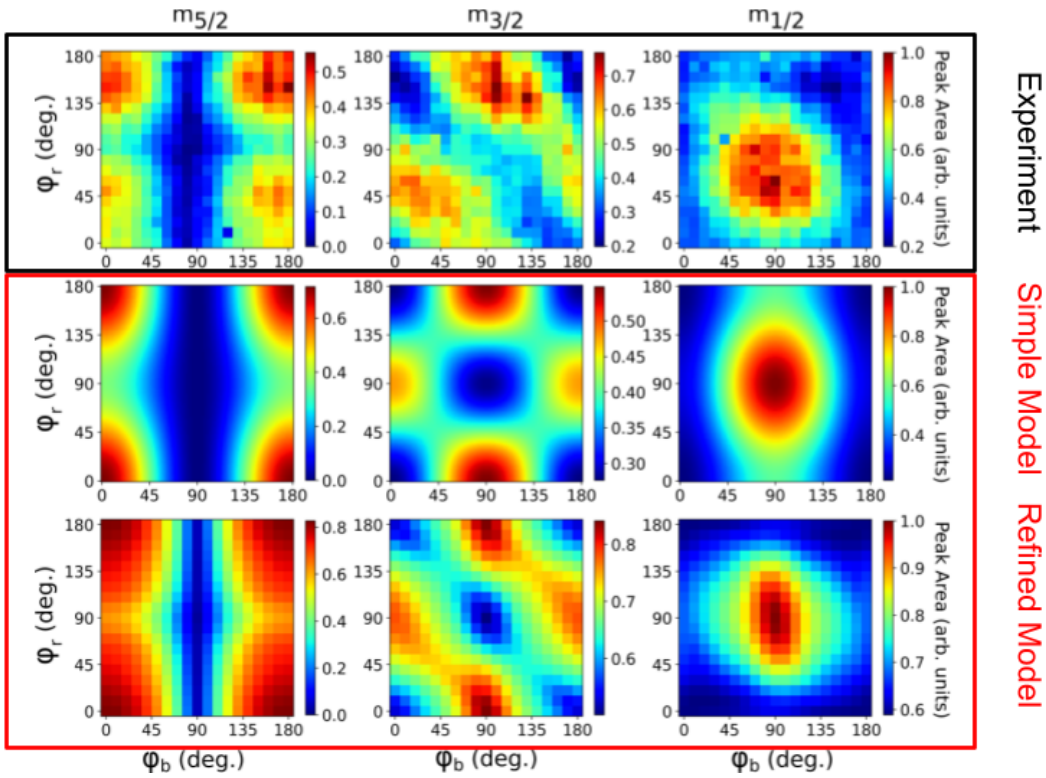

Figure 4.4: At the top, we observe the experimental angular map of m_J sublevel peak heights at each orientation of the probe and coupling fields. Below the experimental data lies an angular map constructed from the simple atomic model. On the bottom lies the angular colormap output of the sophisticated, full atomic model produced by MITRE.

$m_J = \pm 5/2$ resonance is maximized when ϕ_b and ϕ_r are equal to 0° or 180°, and disappear around $\phi_r = \phi_b = 90°$. Conversely, the $m_J = \pm 1/2$ resonance is maximized near $\phi_r = \phi_b = 90°$ and minimized when ϕ_b and ϕ_r are equal to 0° or 180°. When polarization orientations are non-parallel, we see a wide variety of amplitude values. Fig.4.4 depicts simplified atomic model predictions. These modeled color maps can be compared directly with our experimental results. We observe qualitative similarity between the measured angular maps of the $m_{1/2}$ and $m_{5/2}$ sublevels and the simplified atomic model. For $m_J = \pm 5/2$, peak amplitude is maximized where laser polarizations are nearly-parallel with each other and is nearly perpendicular with the

electric field direction in both our model and experiment. Additionally, we observe that $m_J = \pm 1/2$ is minimized in this configuration in both the model and experiment. However, we note that there is a small discrepancy between our model and experimental predictions about the maximized orientation of the $m_J = \pm 1/2$ peak amplitude. This discrepancy may be attributable to a slight ellipticity in our input laser polarization, or an inhomogeneity in the applied electric field. However, the most notable disagreement between model and experiment pertains to the behavior of the $m_J = \pm 3/2$ resonance. This is a clear marker of deficiency in our simple atomic model.

As a result, we primarily utilize the $m_J = 5/2$ and $m_J = 1/2$ resonances when comparing our simple model with experiment. The bottom row of Fig. 4.4 shows the colormap output from the full atomic model constructed by our MITRE collaborators. This sophisticated model matches our experimental data much more closely than the simple model, particularly on the $m_{3/2}$ map. Improved qualitative agreement with a more accurate model inspires confidence in the integrity of our experimental results and invites the possibility of vector field reconstruction via comparison between experiment and model output.

A more viable experimental realization of rotating the electric field angle is shown in Fig.4.5, where laser polarizations are rotated together. These measurements have stronger qualitative alignment with our atomic model. While we do not yet have the capability to demonstrate quantitative sensitivity, these efforts clearly show our capability to qualitatively describe electric field variation with uniform field. Specifically, since the maxima and minima of relative amplitudes for each m_J sublevel are largely aligned between model and experiment, we can use these relative amplitudes to determine our ϕ angle between polarization and electric field orientation. In the case of a uniform field, the ability to determine ϕ from relative sublevel amplitudes

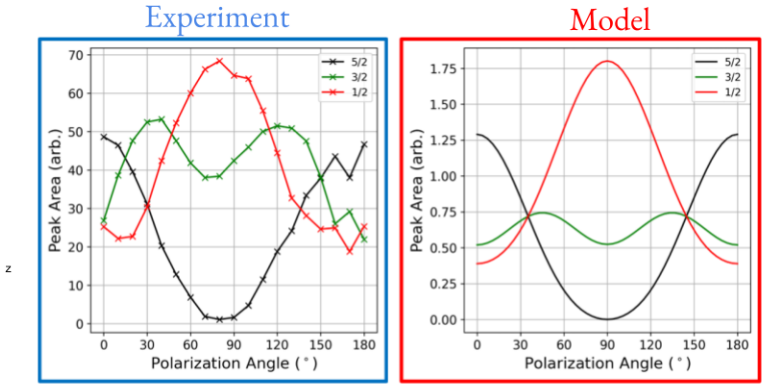

Figure 4.5: Comparison between our experiment and atomic model in the case where polarizations are rotated together ($\phi_b = \phi_r$). Strong qualitative agreement is observed between the experimental results and model output. Since locations of the relative maxima and minima of our sublevels is relatively consistent between our model and experiment, we believe that this comparison will be the basis for field direction reconstruction in the uniform field case.

is sufficient for full field reconstruction.

Chapter 5

Spatially Varying Field Experiments

Having demonstrated full vector reconstruction in the uniform field case, we now consider more complex conditions that more closely resemble real-world applications. Many of the applications of DC Rydberg electrometry involve environments with spatially varying electric fields, such as those found within turbulent plasmas or near powerful particle accelerator beams [4]. In order to extend our approach to the spatially-varying field case, a new technique is necessary. In this chapter, we begin by observing that transmission measurements are no longer viable under these conditions, and that full vector reconstruction now requires measuring two angles (ϕ and θ) rather than just ϕ as in the uniform case. These changes necessitate a different experimental approach. We detail the fluorescence measurement technique as an alternative for capturing spatially-varying information. We again demonstrate qualitative agreement between our experimental results and the output from our simple atomic model.

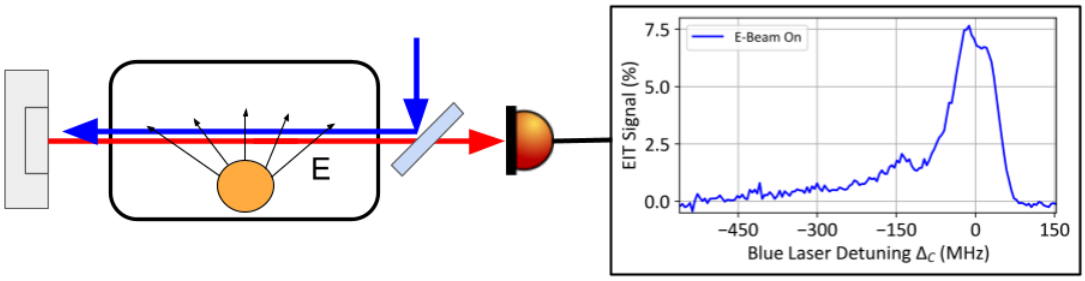

Figure 5.1: Transmission measurements are no longer viable when we consider a spatially varying electric field. In the spatially varying case, each point along the beam path records a different electric field magnitude and direction. Transmission measurements integrate over the beam path, losing this this spatial information. As a result, a different method is needed.

5.1 Fluorescence Detection

A spatially varying electric field differs in magnitude and/or direction across the path of the probe and coupling laser fields. Since transmission measurements integrate the contribution of all Rb atoms across the beam path, they fail to capture spatially varying field information (See Fig. 5.1). As a result, an alternative approach is needed.

Atomic excitation occurs over finite time scales. Eventually, an excited atom "decays" back to the ground state, releasing a photon corresponding to the transition energy in a random direction. In the 3-level EIT ladder scheme, the decay of atoms from the intermediate state to the ground state releases photons at a rate proportional to the intermediate state population. When the two-photon resonance condition is

met and the dark state is achieved, the intermediate state is inaccessible to atomic populations. As a result, fluorescence is suppressed when the probe and coupling laser fields are on resonance. This produces a "dip" in fluorescence corresponding to the two-photon resonance condition. Since photons from this decay are released in all directions, we are able to place our photodetection device perpendicular to the beam path, enabling simultaneous imaging across the beam path. This technique is known as fluorescence detection (See Fig.5.2).

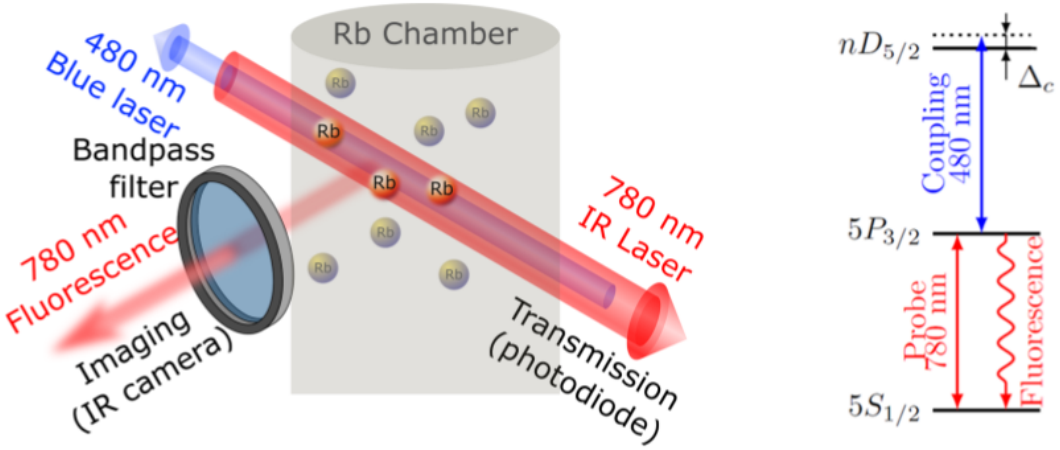

Figure 5.2: An alternative to transmission measurement is fluorescence detection. By measuring photons from atomic decay from the $|e\rangle \rightarrow |g\rangle$ transition, fluorescence imaging enables measurement via a camera that is perpendicular to the beam path. This allows for spatial imaging.

5.2 Experimental Configuration

To explore our sensitivity to electric field variation along the laser propagation direction, we employ a modified setup for fluorescence image detection, depicted in

Fig.5.3a. To produce a spatially varying field for our fluorescence technique, we insert a retractable probe within the vacuum chamber that is 1.4 centimeters in length and 0.8mm in diameter. The wire is placed near the counter-propagating laser beams, producing a spatially varying electric field that is generated when a voltage is applied to the wire. For our measurements, a FLIR camera is placed perpendicular to the propagation direction of the beam. Our observed fluorescence consists of photons emitted by Rb-85 atoms within the vapor cell whenever they decay from the intermediate ($5P_{3/2}$) state back to the ground state. This emitted photon has a wavelength of approximately 780nm, corresponding to the energy associated with the optical transition between the two states. Accordingly, a wavelength filter is placed front of our fluorescence imaging camera to ensure that only 780nm photons are recorded. For our fluorescence measurements we rotate our probe and coupling field polarizations together, producing a single laser polarization orientation ϕ_L. This field is probed using a fluorescence based measurement technique, which is used to construct spatial fluorescence maps. These maps are fitted with Stark maps from ARC at each position along the propagation direction of the beam, which enables magnitude reconstruction of a spatially varying electric field. Fig. 5.3(c)-(e) presents examples of EIT fluorescence spectra and the associated electric field strength at different wire positions. In (c), the wire is placed directly above the laser beams ($\Delta y = 0$. In (d), the wire is retraced by 5mm, and in (e) the wire is retracted by 10mm. In order to compare a roughly equivalent maximum electric field magnitude, the applied voltage was adjusted for each measurement position. The highest electric field magnitude variation is observed closest to the laser beams. This observed variation decreases as the wire position is moved away from the beams.

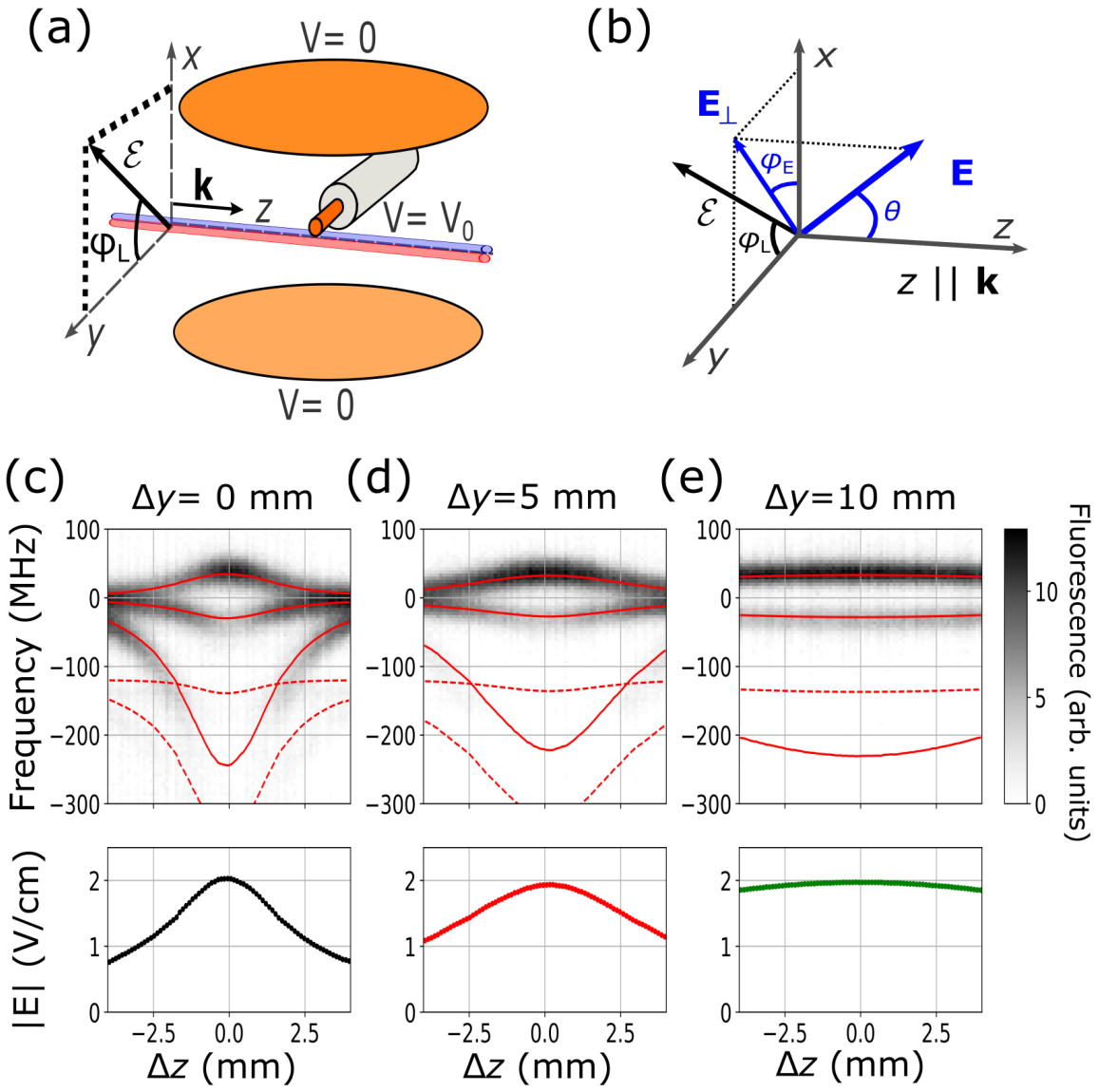

Figure 5.3: (a) Experimental setup for spatially varying measurements, with a retractable probe providing the electric field. (b) Geometry associated with our setup. The perpendicular component of electric field direction is given by ϕ_E, while the parallel directional component is θ. (c) - (e) Fluorescence spectra with the probe placed at varied distances from the counter-propagating lasers, as well as the calculated $\hat{E}$ field magnitude.

5.3 Fluorescence Measurements

For all of our experiments, capacitor plates are needed to generate an electric field, and since we cannot block the beam path, the plates must be placed such that the electric field is generated in the same plane as θ.

As a result, the variation in electric field direction along the laser beam primarily occurs in the longitudinal direction. This variation depends on the horizontal distance Δy between the wire and laser beam. Since our fluorescence monitoring region is the same range across the propagation direction for each position measurement, we expect to record smaller θ variation when the wire is further from the lasers [6]. Because the longitudinal component of the electric field does not fundamentally change the polarization dependence of EIT peaks, measurement of θ is more challenging. Reducing the angle between the electric field and the laser beams makes polarization dependence less pronounced, which eventually eliminates polarization dependence as $\theta \to 0$. For our experimental arrangement, we would expect the $m_J = \pm 1/2$ peak to be strongest when $\theta = 90^\circ$ and then become smaller with decreasing θ. In Figure 5.4 (b), we observe the experimental dependence of the $m_J = \pm 1/2$ EIT peak area along the laser beam. Figure 5.4 (d) displays the results of our atomic model calculations of this situation. We observe general alignment with expected behavior. Measured resonance peak areas are largest corresponding with $\theta \approx 90^\circ$. Each position has similar shapes, but cover a different range of angles. We observe that the $\Delta y = 5$mm and $\Delta y = 10$mm positions match our atomic model predictions well. Some deviation from the model is observed in the $\Delta y = 0$ position, which is likely attributable to some combination of imperfection in the wire or the presence of field gradients. It is also possible that our assumption of the wire as a point charge breaks down when it is positioned in close proximity to our laser beams. Nonetheless, all positions follow the

expected dependence. With better calibration it should be possible to use EIT resonance analysis to reconstruct full vector information of inhomogenous electric fields.

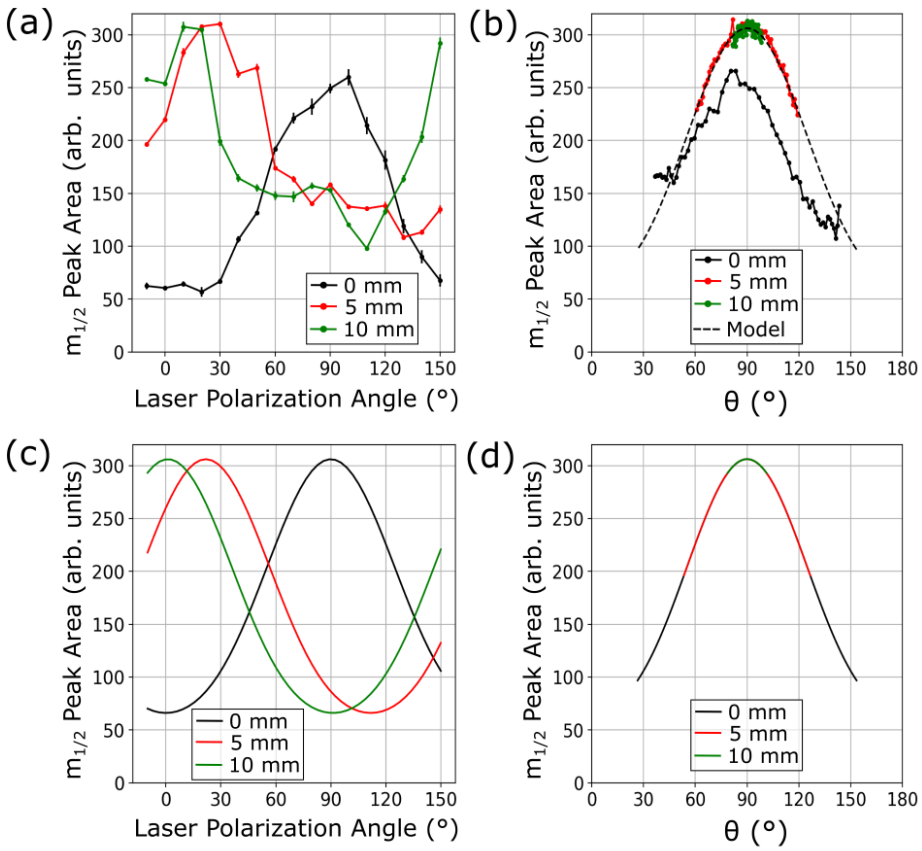

Figure 5.4: Variation of θ and ϕ electric field for different wire positions. (a) Experimental data for $m_{1/2}$ peak area at different probe positions. We observe shifts in the maximum position of the $m_{1/2}$ peak depending on probe position. (b) Theta sensitivity of $m_{1/2}$ peak data for different probe positions with a fixed polarization. Reduced theta sensitivity is observed when wire is positioned further is from the laser beams. (c) The atomic model response of $m_{1/2}$ peak area for different probe positions. (d) Atomic model response for different probe positions with a fixed polarization angle. Good qualitative alignment is observed between theory and experiment for these measurements

Chapter 6

Introducing a Magnetic Field

In this chapter, we describe the incorporation of a magneticc field into our uniform field experiment. We detail the changes to the setup made to incorporate magnetic input, and underline the improvements of our measurements that this addition offers.

6.1 Theoretical Overview

The magnetic analog of the Stark Effect is known as the Zeeman Effect [5]. The Zeeman detuning of a given atomic transition is given by:

$$\Delta E = g_L \mu_B m_J B \tag{6.1}$$

where g_L is the Lande g-factor, μ_B is the Bohr magneton, m_J is the magnetic quantum number, and B is the magnitude of the applied magnetic field. The Zeeman effect describes a linearly proportional relationship between detuning from the central resonance and magnetic field strength. On an EIT spectra, this manifests as a separate detuned resonance corresponding with each m_J number (See Fig. 6.1). For our purposes, the application of a fixed, known magnetic field enables us to establish a quantization axis separate from the electric field orientation. This distinct quantization axis enables us to break the symmetry that is evident from measurements in Fig. 4.4, and should facilitate more accurate measurement of electric field strength.

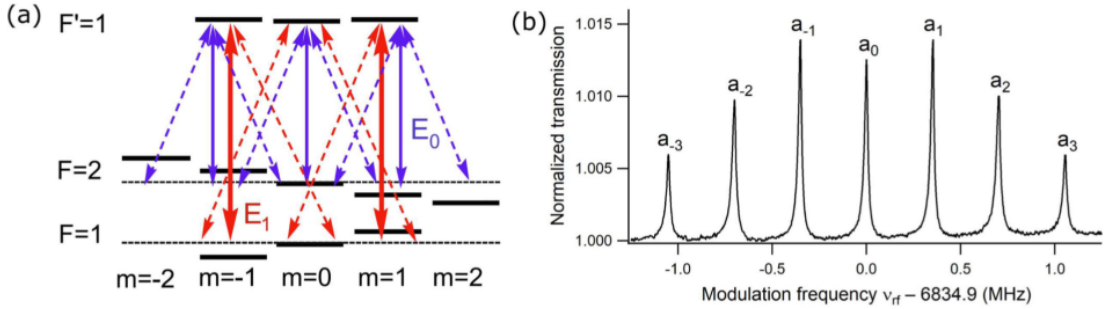

Figure 6.1: This figure from Maldonado et al. [5] The relationship between magnetic field strength and optical detuning of EIT peaks is described by the Zeeman effect [5]. An applied magnetic field produces 7 peaks, 6 of which detune from the central resonance proportional with magnetic field strength.

6.2 Experimental Setup

The setup employed for this experiment is a modified version of Fig. 4.1, with capacitor plates replaced by an electrode that is inside of the vapor cell (See Fig. 6.2(a)). The plate separation within the vapor cell is 5mm, and the cell length is approximately 50mm. This modified vapor cell enhances measurement precision, replacing the rotation of the probe and coupling field's polarization with direct rotation of the applied electric field. The electrode cell is placed upon on the apparatus shown in Fig. 6.2, which enables rotation of the electric field with 1° precision. Magnetic field is generated by a pair of Helmholtz coils. The Helmholtz coil pair is configured such that the cell is in the center of the coils, at a distance of the coil radius from each.

6.3 Measurement

In this configuration transmission spectra are recorded with an identical procedure to the uniform electric field case. Figure 6.3(a) depicts the results of measurements from our electrode cell without an applied magnetic field. These spectra closely

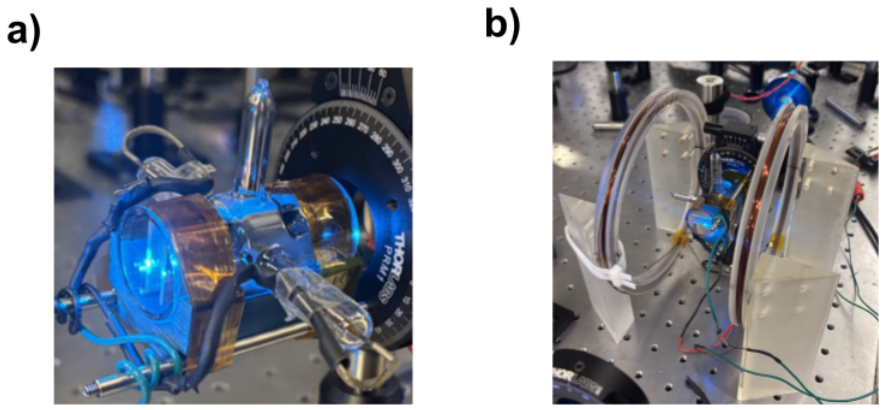

Figure 6.2: (a) depicts the electrode cell that enables more precise measurement. Rather than relying on modifying polarization angle to change laser field orientation relative to electric field, the electrode cell can be rotated to directly change electric field orientation. The cell is secured to a waveplate rotation stand to enable precise rotation of the electric field. (b) depicts the electrode cell on its rotating stand, with a pair of Helmholtz coils positioned around it. By placing the cell at the center of Helmholtz coils, a relatively homogenous magnetic field can be applied. In this image, the field is applied in the y-direction. A set of 3 Helmholtz coils could enable 3-dimensional magnetic field application.

mirror the spectra taken from the vacuum chamber setup. In particular, we notice the $m_J = 5/2$ peak clearly present when $E \perp \epsilon_{r,b}$, and completely absent when $E \parallel \epsilon_{r,b}$. Additionally, the peaks appear cleaner than in the prior setup. This is likely due to the reduced electric field gradients within the electrode cell as compared with the larger vacuum chamber, which had more potential for charging effects.

Next, a fixed magnetic field was produced by applying a current to the Helmholtz coil pair. The polarization of the probe and coupling fields were also fixed. A series of measurements were taken over the range $-90° \leq \phi_E \leq 90°$, in $5°$ increments with $0°$ defined as $E \parallel B$. The results of this measurement is shown in Figure 6.3b. We observe clear splitting of the fine structure due to changes in electric field orientation. Importantly, this splitting can be observed in the frequency domain. This development facilitates greater precision in determining peak direction, as we are able to infer ϕ information via the peak detuning technique illustrated in Fig. 4.3a, rather than relying on an imprecise peak-area fitting method. This should drastically improve measurement precision, making this technique more viable for real-world application.

It is important to note that this technique does not address the issues in accurately determining θ orientation. We are unable to generate electric field in the longitudinal direction, since placing electrodes in this manner would block our beam. As a result, the applied magnetic field technique is currently limited to the uniform-field case.

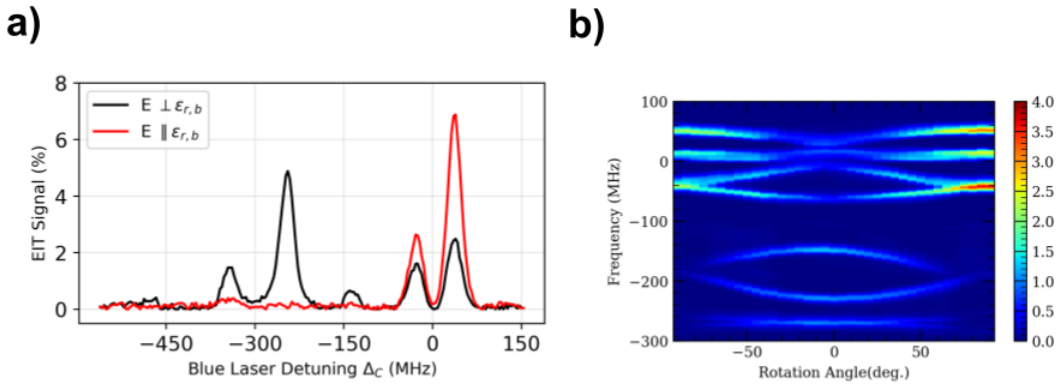

Figure 6.3: (a) depicts electric field sensitivity measurements, similar to those shown in Fig. 4.2, conducted using the electrode cell. Successful electric field responsiveness is observed. The measurements in (b) the electrode cell on its rotating stand, with a pair of Helmholtz coils positioned around it. By placing the cell at the center of Helmholtz coils, a relatively homogenous magnetic field can be applied. In this image, the field is applied in the y-direction. A set of 3 Helmholtz coils could enable 3-dimensional magnetic field application.

Chapter 7

Conclusion and future steps

In this project, we strove to develop a method for full vector reconstruction of the electric field. To realize this measurement, we excite alkali metal atoms to the Rydberg state, and then produce the two-photon coherent effect known as Electromagnetically Induced Transparency. We demonstrate the use EIT spectroscopy for these vector field measurements.

The first part of our experiment considered the case of a uniform electric field. In this case, transmission measurements were recorded on a photodetector. By monitoring peak detuning and peak area, we are able to measure magnitude and ϕ information, respectively. Our directional dependence aligns qualitatively with our model, though sensitivity estimates have not yet been achieved.

In the second part of our experiment, we introduce fluorescence detection as a means of observing a spatially varying electric field. By manipulating the position of a retractable wire, we are able to generate an electric field that varies both ϕ and θ orientation. We demonstrate sensitivity to phi-dependence of peak area, and observe variation in electric field magnitude that corresponds with theta variation. Ultimately, this fluorescence imaging technique provides an avenue to full, non-invasive vector field reconstruction in the spatially varying field case.

Lastly, we introduce a magnetic field as a means of establishing a quantization

axis independent of electric field direction. Our preliminary results show that this technique enables us to determine electric field direction from detunings in the frequency domain, rather than a measurement of peak area. This technique provides the potential for easier, more precise measurement of vector electric field information.

This project suggests significant potential for Rydberg-based non-invasive electric field sensing. Future experimentation in line with this project would include a conclusive sensitivity estimation for our measurements in each experimental configuration. Moreover, there is the potential to incorporate structured light into the experiment through the introduction of a vortex waveplate which could enable imaging 360° of light polarization simultaneously.

References

[1] John S. Belrose. "Reginald Aubrey Fessenden and the Birth of Wireless Telephony". In: *IEEE Antennas and Propagation Magazine* 44.2 (Apr. 2002). File copy of original manuscript, pp. 38–47. URL: https://www.radiocom.net/Fessenden/Belrose.pdf.

[2] Christopher L. Holloway et al. "Overview of Rydberg Atom-Based Sensors/Receivers for the Measurement of Electric Fields, Power, Voltage, and Modulated Signals". In: *Antenna and Array Technologies for Future Wireless Ecosystems*. Ed. by Y. Jay Guo and Richard W. Ziolkowski. NIST publication copy of a book chapter. Boulder, CO, USA: John Wiley & Sons, Inc., 2022. Chap. 11, pp. 393–417. URL: https://tsapps.nist.gov/publication/get_pdf.cfm?pub_id=932793.

[3] Jefferson Lab. *Harps for Dummies*. https://www.jlab.org/accel/beam_diag/harp/harp_dummy.html. Jefferson Lab Accelerator Beam Diagnostics. 2004.

[4] Mykhailo Vorobiov et al. *Non-perturbative 2D spatial measurements of electric fields within a plasma sheath*. 2025. arXiv: 2511.12322 [physics.plasm-ph]. URL: https://arxiv.org/abs/2511.12322.

[5] Mario Gonzalez Maldonado et al. "Sensitivity of a vector atomic magnetometer based on electromagnetically induced transparency". In: *Opt. Express* 32.14 (July 2024), pp. 25062–25073. DOI: 10.1364/OE.529276. URL: https://opg.optica.org/oe/abstract.cfm?URI=oe-32-14-25062.

[6] Rob Behary et al. *Static dc electric field orientation effects on two-photon Rydberg EIT*. 2026. arXiv: 2601.09676 [physics.atom-ph]. URL: https://arxiv.org/abs/2601.09676.

[7] Fabian Olbrich. *Rydberg Atoms*. Hauptseminarvortrag, University of Stuttgart. Lecture notes / seminar presentation. June 2013. URL: https://www.itp3.uni-stuttgart.de/downloads/physikderkaltengase/14_Rydberg_Fabian_Olbricht.pdf.

[8] N. Šibalić et al. "ARC: An open-source library for calculating properties of alkali Rydberg atoms". In: *Computer Physics Communications* 220 (Nov. 2017), pp. 319–331. ISSN: 0010-4655. DOI: 10.1016/j.cpc.2017.06.015. URL: http://dx.doi.org/10.1016/j.cpc.2017.06.015.

[9] Nathan C. Song. *Nonlinear Quantum Optics with Rydberg Atoms*. Undergraduate Final Project, University of California, Berkeley. Accessed: 2026-03-22. 2024. URL: https://nsong03.github.io/resources/Phys130FinalProject.pdf.

[10] Vladimir Dzuba. "Calculation of Polarizabilities for Atoms with Open Shells". In: *Symmetry* 12.12 (2020). ISSN: 2073-8994. DOI: 10.3390/sym12121950. URL: https://www.mdpi.com/2073-8994/12/12/1950.

[11] N. Šibalić et al. "ARC: An open-source library for calculating properties of alkali Rydberg atoms". In: *Computer Physics Communications* 220 (2017), pp. 319–331. ISSN: 0010-4655. DOI: https://doi.org/10.1016/j.cpc.2017.06.015. URL: https://www.sciencedirect.com/science/article/pii/S0010465517301972.

[12] Felix Klein. *The mathematical theory of the top: Lectures delivered on the occasion of the sesquicentennial celebration of Princeton University*. New York: C. Scribner's Sons, 1897. URL: https://archive.org/details/mathematicaltheo00kleiuoft.